Nuclear Instruments and Methods in Physics Research A 1062 (2024) 169224

Contents lists available at ScienceDirect

Nuclear Inst. and Methods in Physics Research, A

journal homepage: www.elsevier.com/locate/nima

Full Length Article

A Compton transmission polarimeter for DC and SRF electron photo-injectors

G. Blume [a,*], M. Bruker [b], C. Cuevas [b], H. Dong [b], Benjamin Fernandes Neres [c], P. Ghoshal [b], S. Gopinath [b], J. Grames [b], S. Gregory [b], G. Hays [b], C. Le Galliard [c], S. Marsillac [a], B. Moffit [b], Thi Nguyen Trung [c], M. Poelker [b], R. Suleiman [b], E. Voutier [c], S. Zhang [b]

[a] Department of Physics, Old Dominion University, Norfolk, VA, 23529, USA
[b] Thomas Jefferson National Accelerator Facility, Newport News, VA, 23606, USA
[c] Université Paris-Saclay, CNRS/IN2P3, IJCLab, 91405, Orsay, France

ARTICLE INFO

Keywords:
Compton transmission polarimetry
Mott-scattering polarimetry

ABSTRACT

A polarimeter was constructed to measure the longitudinal polarization of a spin-polarized electron beam at 5 and 7 MeV. The polarimeter takes advantage of Compton scattering between circularly polarized bremsstrahlung photons produced by a longitudinally polarized electron beam striking a copper radiator and the spin-polarized electrons orbiting the iron atoms of an analyzing magnet. This so-called Compton transmission polarimeter is compact and relatively inexpensive compared to Mott-scattering polarimeters because no spin manipulator is required. This work presents the design of the radiator, analyzing magnet, photon detector assembly, and data acquisition system of the Compton transmission polarimeter as well as beam commissioning results performed at the Upgraded Injector Test Facility at Jefferson Lab.

1. Introduction

Today, all accelerator-based physics programs that provide spin-polarized electron beams rely on DC high voltage photoguns with GaAs-based photocathodes. Mott-scattering polarimetry is the typical method of choice for providing accurate polarization measurements, with viable polarimeter designs described in the literature for measurement at the gun bias voltage [1–4] and at post-acceleration energy up to about 14 MeV [5,6]. Mott scattering is appealing because its analyzing power (see Appendix) can be very high, approaching 50%. However, one drawback is the requirement for transverse polarization at the scattering target. Since the polarization direction for electrons originating from a GaAs-based photocathode is longitudinal to the direction of motion, a spin rotator is required. Spin rotators can be complicated, expensive, and can occupy a significant portion of the beamline [7,8].

The Compton transmission polarimeter represents an alternative to Mott-scattering polarimetry. The analyzing power is much smaller – of the order 1% – but the method offers advantages that include comparative simplicity and sensitivity to longitudinal polarization. As a result, a spin rotator is not necessarily required, depending on the placement of the device. Additionally, the method can be employed over a very broad range of beam energy, up to ∼ 1000 MeV [9–12], where electron polarimetry can be technically complicated [13,14].

The development of the Compton transmission polarimeter described in this paper is motivated by a collaboration between Jefferson Lab, Fermi National Accelerator Laboratory, Brookhaven National Laboratory (BNL), and Stony Brook University, which aims to produce a polarized electron beam from a superconducting radio-frequency (SRF) photogun for the first time. Historically, this has been difficult because GaAs-based photocathodes are very fragile, requiring extremely good vacuum in order to maintain the required negative-electron-affinity condition at the surface of the photocathode. SRF photoguns generally possess good vacuum; however, it is not uncommon for SRF guns to exhibit field emission, particularly at the location of the photoemitter, which for the case of GaAs is not superconducting. Brief exposure to the gas load caused by field emission or multipacting can quickly degrade the quantum efficiency (QE) of a GaAs photocathode. However, the BNL SRF quarterwave resonator was designed to minimize field emission, particularly at the location of the photocathode. Of all SRF photogun programs, the BNL SRF quarterwave resonator design has demonstrated the best operating performance, setting records for average current and bunch charge [15,16].

The beam energy from the BNL SRF quarterwave photogun in the Coherent electron Cooling (CeC) accelerator with a GaAs photocathode is 1.25 MeV, with acceleration up to 14.5 MeV using a "booster" cryomodule located a few meters from the gun [17]. This energy and

* Corresponding author.
E-mail address: gtblume@jlab.org (G. Blume).

https://doi.org/10.1016/j.nima.2024.169224
Received 2 November 2023; Received in revised form 9 February 2024; Accepted 28 February 2024
Available online 6 March 2024

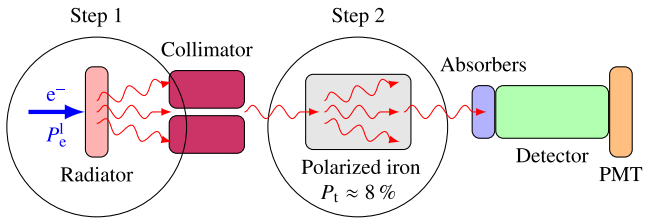

Fig. 1. Concept of a Compton transmission polarimeter. Here, an incident electron beam carries a longitudinal polarization P_e^l, which produces circularly polarized bremsstrahlung photons upon striking a radiator. These photons are then collimated before an iron target with polarization P_t where the photons undergo polarized Compton scattering. Different electron-beam helicities produce an asymmetry that can be observed in a subsequent detector consisting of a scintillating crystal and PMT. Once the analyzing power is calibrated, measuring the asymmetry provides a measurement of the beam polarization.

the limited space available do not permit the use of a spin rotator required by Mott-scattering polarimetry. As such, Compton-transmission polarimetry is the only viable option.

In this paper, we describe the method and operation of Compton transmission polarimetry. Then, we outline the calibration of the polarimeter at the energies planned to be used with the BNL SRF gun at the CeC, i.e., 5 and 7 MeV. Using a known electron-beam polarization determined by a Mott polarimeter at 180 keV, we report an effective analyzing power of 1.2% at these energies. Finally, using the effective analyzing power determined experimentally and a GEANT4 Monte-Carlo simulation of the analyzing magnet [18–20], we predict polarimeter behavior for beam systematic studies. The approach outlined here can be extended to other accelerator initiatives including polarimetry for polarized-positron source development at Jefferson Lab, for which a Mott-scattering polarimeter is not necessarily feasible [21, 22].

2. Polarimeter design

Compton transmission electron polarimetry is a two-step process shown schematically in Fig. 1. First, polarized electrons with longitudinal polarization are incident on a radiator. The bremsstrahlung photons produced within the radiator are elliptically polarized, with a degree of circular polarization dependent on the degree of electron polarization. As is typical, the direction – or helicity – of the electron-beam polarization can be flipped parallel or anti-parallel to the direction of the beam motion using a Pockels cell located on the drive laser table [23]. In this manner, the polarization of the bremsstrahlung photons flips between right and left circular.

Next, the circularly polarized bremsstrahlung photons are incident on an iron target that is polarized using a solenoidal magnetic field with a switchable field direction aligned parallel or anti-parallel to the direction of electron beam motion. The circularly polarized bremsstrahlung photons Compton-scatter from the spin-polarized electrons of the iron atoms, with different scattering probability depending on the helicity state of the polarized bremsstrahlung photons, which results in different transmission levels for the bremsstrahlung photons passing through the iron. These steps are presented mathematically below.

The interaction of circularly polarized photons with the longitudinally polarized electrons of the analyzing target (P_t) is described by the cross section [24]

$$\frac{d^2\sigma}{d\Omega} = \frac{d^2\sigma^0}{d\Omega}\left[1 + P_t P_\gamma^c A_C(\theta)\right] \tag{1}$$

where $d^2\sigma^0/d\Omega$ is the unpolarized Compton cross section [25]

$$\frac{d^2\sigma^0}{d\Omega} = \frac{1}{2}\left(r_0\frac{\omega}{\omega_0}\right)^2\left[\frac{\omega_0}{\omega} + \frac{\omega}{\omega_0} - \sin^2(\theta)\right], \tag{2}$$

and

$$A_C(\theta) = \left[\frac{\omega_0}{\omega} - \frac{\omega}{\omega_0}\right]\cos(\theta)\Big/\left[\frac{\omega_0}{\omega} + \frac{\omega}{\omega_0} - \sin^2(\theta)\right] \tag{3}$$

is the analyzing power of the Compton process, both quantities depending on the energy ω and the angle θ of the scattered photon, and the energy ω_0 of the incident photon [26,27]. Considering the case of a monochromatic parallel photon beam scattering off electrons in an analyzing magnet of length L, the transmission efficiency characterizing the probability that a photon exits the target may be written as

$$\varepsilon_T = \exp\left[-(\mu_0 + \mu_1 P_t P_\gamma^c)L\right], \tag{4}$$

which assumes the loss of any photon interacting in the target and the dominance of the Compton process; μ_0 and μ_1 are the energy-dependent unpolarized and polarized Compton absorption coefficients

$$\mu_0 \equiv \mu_0(\omega) = \rho_e \int d\Omega\, \frac{d^2\sigma^0}{d\Omega} \tag{5}$$

$$\mu_1 \equiv \mu_1(\omega) = \rho_e \int d\Omega\, \frac{d^2\sigma^0}{d\Omega} A_C(\theta) \tag{6}$$

with ρ_e the electron density of the target material. The measurement of the circular polarization of the photon beam is obtained from the number of transmitted photons for opposite magnet polarity or photon polarization orientations. The corresponding asymmetry is written

$$A_T = \frac{N^+ - N^-}{N^+ + N^-} = \tanh(-P_t P_\gamma^c \mu_1 L) \approx -P_t P_\gamma^c \mu_1 L, \tag{7}$$

from which the circular polarization of the photon is inferred following

$$P_\gamma^c = -A_T/\mu_1 P_t L, \tag{8}$$

where $\mu_1 P_t L$ is the effective analyzing power of the polarimeter, which is its sensitivity to photon circular polarization.

The Compton polarimeter extends this operating principle to a polarized electron beam by measuring the polarization of the photon spectra generated by the bremsstrahlung of the electron beam into a radiator. In that process, the longitudinal polarization of electrons proportionally transfers into a circular photon polarization, i.e.,

$$P_\gamma^c \equiv P_\gamma^c(\omega_0) = P_e^l \mathcal{T} \tag{9}$$

where $\mathcal{T} \equiv \mathcal{T}(\omega_0)$ is the energy-dependent polarization transfer [28,29]. The response of a photon detector placed after the analyzing target can be represented analytically [30] by the helicity ($\pm$) dependent average transmission efficiency

$$\langle\varepsilon_T^\pm\rangle = \int_0^T d\omega\, d\Omega\, \frac{d\sigma_b}{d\omega\, d\Omega}\, e^{-\mu_t^\pm L}\Big/\int_0^T d\omega\, d\Omega\, \frac{d\sigma_b}{d\omega\, d\Omega} \tag{10}$$

where T is the kinetic energy of the electron beam, and $d\sigma_b/d\omega\, d\Omega$ is the 3-fold bremsstrahlung differential cross section. The total absorption coefficient

$$\begin{aligned}\mu_t^\pm \equiv \mu_t^\pm(\omega) &= \mu_{\gamma e} + \mu_{e^+e^-} + \mu_0 \pm \mu_1 P_e^l P_t \mathcal{T} \\ &= \mu_t^0 \pm \mu_1 P_e^l P_t \mathcal{T}\end{aligned} \tag{11}$$

takes into account the energy-dependent photoelectric (γe) and pair creation (e^+e^-) processes which also contribute to the disappearance of photons. More than a photon counter, the detector absorbs the total energy deposited by transmitted photons over a period of time corresponding to the duration of a single electron helicity state, that is

$$\langle E_T^\pm\rangle = \int_0^T d\omega\, d\Omega\, \frac{d\sigma_b}{d\omega\, d\Omega}\, \omega e^{-\mu_t^\pm L}\Big/\int_0^T d\omega\, d\Omega\, \frac{d\sigma_b}{d\omega\, d\Omega}. \tag{12}$$

The polarization-dependent part of the photon absorption is small enough that

$$e^{-\mu_t^\pm L} \approx e^{-\mu_T^0 L}\left(1 \pm \mu_1 P_e^l P_t \mathcal{T} L\right). \tag{13}$$

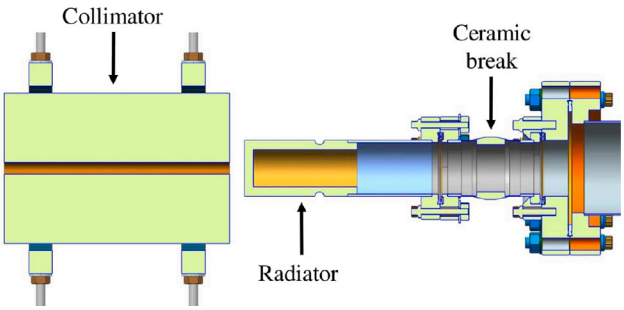

Fig. 2. Cross-section view for the radiator and collimator. Beam travels right to left.

Comparing signals of opposite helicities, the experimental asymmetry can be written

$$A_E = P_e^l P_t L \frac{\int_0^T d\omega\, d\Omega\, \frac{d\sigma_b}{d\omega\, d\Omega}\, \omega e^{-\mu_t^0 L}\, \mu_1 \mathcal{T}}{\int_0^T d\omega\, d\Omega\, \frac{d\sigma_b}{d\omega\, d\Omega}\, \omega e^{-\mu_t^0 L}}$$
$$= P_e^l P_t \langle \mu_1 \mathcal{T} \rangle L = P_e^l P_t A = P_e^l \mathcal{A}_{\text{eff}}, \quad (14)$$

where $\mathcal{A}_{\text{eff}}$ describes the effective analyzing power of the polarimeter, a quantity that is on the order of 1%.

As the polarization of the electrons in the iron in the magnet is difficult to know *a priori*, Compton transmission polarimeters [9–12] are frequently used to measure "relative" beam polarization. This is true for the work described here too, but because the Compton transmission polarimeter was installed at a test facility – the Upgraded Injector Test Facility at Jefferson Lab – that includes a Mott-scattering polarimeter, a level of quantitative assessment could be achieved. The strategy was to calibrate the new Compton transmission polarimeter against the Mott scattering polarimeter under conditions that mimic the anticipated conditions at the CeC accelerator at BNL.

The first step was to measure electron-beam polarization using the Mott-scattering polarimeter at 180 keV. Then, the beam was delivered to the Compton transmission polarimeter at 5 MeV and 7 MeV (expected beam energy at the CeC accelerator at BNL) to measure the Compton asymmetry A_E and calculate $\mathcal{A}_{\text{eff}}$ using Eq. (14). Finally, we used GEANT4 to simulate the analyzing magnet and estimate A_E for a 100% polarized iron core. The measured $\mathcal{A}_{\text{eff}}$ and simulated A_E can be used to further calibrate the GEANT model for use in optimizing polarimeter use.

The physical construction of the polarimeter is composed of just four elements: a photon radiator, a photon collimator, an analyzing magnet, and a photon detector. The elements are described in detail below.

2.1. Photon radiator and collimator

The spin-polarized electron beam is delivered to a water-cooled radiator made of high-purity copper with thickness 0.60 cm chosen to completely stop an electron beam of 9.5 MeV kinetic energy. The radiator is part of a copper tube soldered to a stainless steel half-nipple with DN40 Conflat flange. The apparatus is electrically isolated by virtue of a ceramic break, thus permitting beam-current measurement.

Downstream of the radiator is a copper photon collimator, 14.6 cm long with inner diameter of 0.8 cm and outer diameter of 10.2 cm. The collimator is used to stop large-angle scattered photons that may reach the detector without passing through the magnet. The radiator and collimator are shown in Fig. 2

2.2. Analyzing magnet

The analyzing magnet (Fig. 3) consists of an iron core (75 mm long, 25.4 mm diameter), a magnetic return path comprised of two iron flanges and a sleeve, and the solenoid coil. All of the iron components,

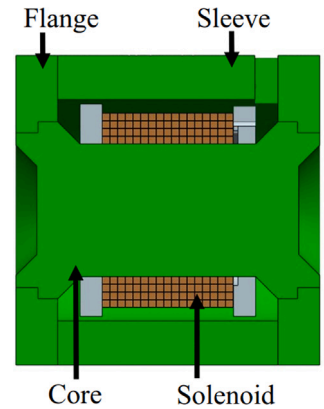

Fig. 3. The polarized magnet showing the geometry of the core, flux return, and coil.

including the core, are made of low-carbon steel (SAE/AISI 1005). The solenoid winding was constructed from four layers of 2.2 mm × 2.2 mm square copper conductor wet-wound around the core and then vacuum-impregnated. Wet winding is the process of immersing the conductor in a ceramic epoxy resin to improve thermal conductivity and avoid mechanical motion of the windings due to Lorentz forces.

The simulation program ANSYS Maxwell [31] was used to optimize the magnet design with the goal of achieving a saturated magnetization along the length of the iron core (i.e., the volume where the bremsstrahlung photons scatter) at a modest operating current (less than 10 A). A saturated field is important such that all target electrons have the same polarization (∼ 8 % for iron [32]). This involved adjusting the mechanical dimensions of each component, particularly the sleeve thickness.

The results of the simulation are shown in Fig. 4. Here, Figs. 4a and 4b show the longitudinal and transverse magnetic field magnitudes as a function of distance along the magnet at 4 different radii. Fig. 4c shows the overall finite element analysis (FEA) model solution at 5 A. Magnetic saturation was achieved with a maximum simulated field of 1.75 T, with the peak field located approximately 15 mm from the front face of the magnet, and maintained for 45 mm before falling off. Approximately 70% of the iron core volume is magnetized to the peak magnetic field (see Fig. 4c). The more computationally intensive modeling program OPERA3D was employed in the final stages of design to ensure accuracy of the ANSYS Maxwell results [33].

Two identical magnets were fabricated and bench-tested for quality control. The magnetic field across the surface of the core and flange was measured at a distance of 1.5 mm to evaluate the leakage field. The leakage fields were found to be less than 10^{-4} of the expected core field (below 5 mT) and in excellent agreement qualitatively with the expected profile due to the mechanical tolerances used in assembly.

The electrical properties of the magnet were measured (3.2 mH and 49 mΩ), and thermal measurements were made of the magnet at twice the nominal operating current. Under sustained operation at 10 A current for 30 h, a peak temperature of 31 °C was measured at the steel sleeve.

A magnet power supply with 10 A and 30 V capability was used for the experiment. The magnet power supply was operated two different ways in order to "train" the iron core magnetization in a consistent manner. The first method was used to restore a desired level of magnetization. Here, the power supply was cycled between ±9.0 A two times, reaching the final current from +9.0 A. For beam tests requiring zero polarization, the second method was employed where the magnet was degaussed by cycling the power supply through both polarities with successively lower currents as shown in Fig. 5.

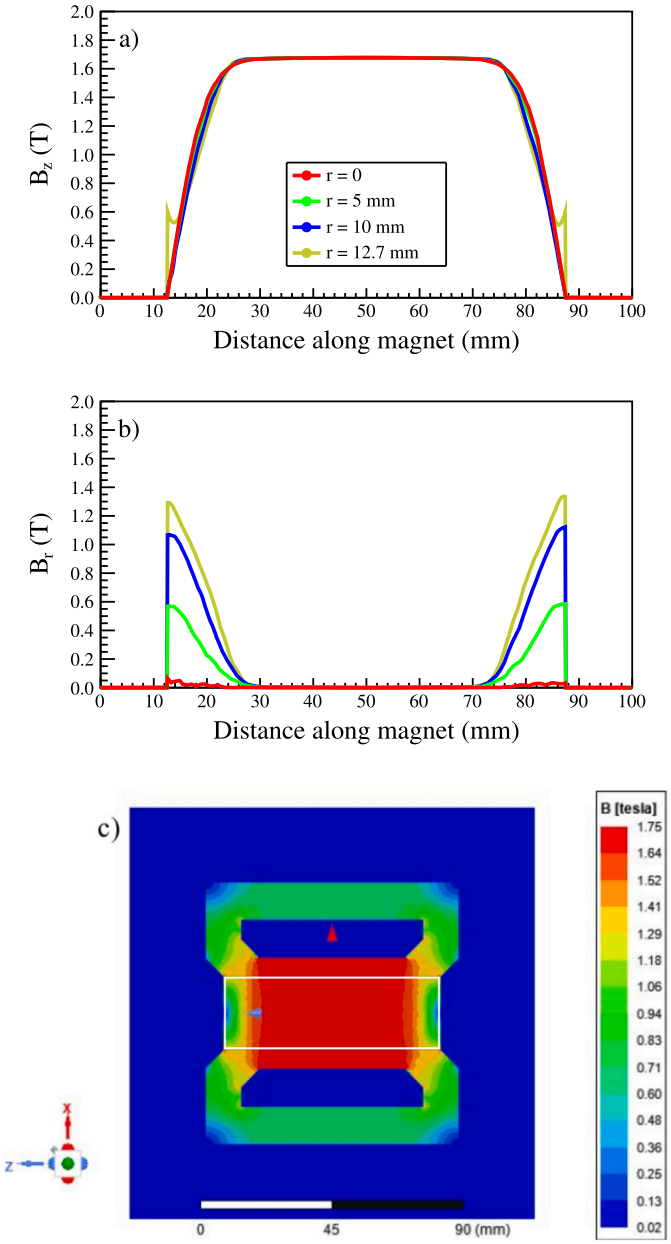

Fig. 4. ANSYS Maxwell output showing the longitudinal (a) and radial (b) field components within the magnet bore (iron core from 12.5 mm to 87.5 mm) along the beam axis across the radius from the axis (r = 0 mm) to the end of the bore (r = 12.7 mm) and inset (c) shows the overall FEA model solution. The core is highlighted in white. Results shown for the magnet modeled at 5 A solenoid operating current.

2.3. Photon detector

The photon detector (shown in Fig. 6) consists of a cylindrical $Bi_4Ge_3O_{12}$ (BGO) crystal [34], 15 cm long and 5 cm in diameter. The crystal was wrapped with 50 μm-thick VM2000 [35] reflective paper and 50 μm-thick Tedlar [36] absorptive black paper; the former wrapping improves the light collection of the intended bremsstrahlung photons that pass through the analyzing magnet, while the latter minimizes the signal produced from unwanted outside light. The optical signal was read by a photomultiplier tube R2154-02 [37] equipped with a passive custom base which ensured high linearity over a large high-voltage domain (500–1700 V). The full assembly was mounted inside a brass box which provided RF and additional light shielding. The

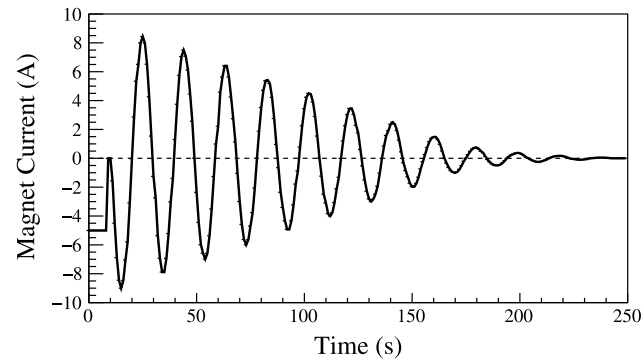

Fig. 5. An example of the degaussing process following operating at −5 A. The current is cycled between a maximum ± 9 A down to 0 A to demagnetize the target.

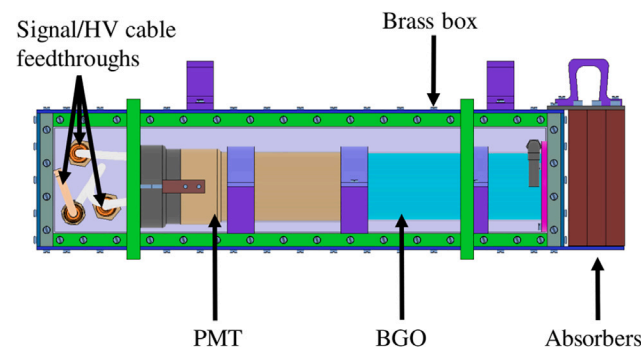

Fig. 6. The photon detector box. The side wall has been removed to show crystal geometry.

front of the box included space for three insertable copper absorbers, each providing signal reduction of 1/2 for a minimum of 1/8 of the maximum photon flux. The absorbers minimize the degradation of the optical properties of the crystal under conditions of very high rates.

3. Experiment

The polarized electron photoinjector at the Upgraded Injector Test Facility (UITF, see Fig. 7) [38] is comprised of several subsystems: a GaAs photoemission gun, a polarized drive laser to create the electron bunches, a Wien-filter spin rotator to orient the spin direction (for Mott polarimeter measurements), several RF cavities to temporally shape the individual electron bunches, a superconducting RF (SRF) cryomodule to accelerate the beam to several MeV [38], conventional steering and focusing magnets, and beam diagnostic elements to evaluate beam characteristics at the radiator of the Compton transmission polarimeter.

The polarized electron gun is an inverted-insulator DC high-voltage electron gun [39] with a load lock to allow photocathode exchange without disturbing the ultra-high vacuum inside the photogun. The photogun operated at 180 keV throughout this experiment and the photocathode was bulk GaAs, providing (37.7 ± 2.3)% polarization as measured by the Mott polarimeter (see Appendix).

The drive laser was operated at 12.37 MHz, the 121st sub-harmonic of the 1.497 GHz cryomodule fundamental frequency. This relatively low-frequency optical pulse train was produced by a gain switched seed laser driven by a DC bias and electrical pulses from a ps pulse generator followed by fiber laser amplifiers [40]. The 1560 nm fundamental laser beam was frequency-doubled to 780 nm to excite electrons at the band gap of bulk GaAs. The linear polarization of the laser beam was converted to circular polarization with a Pockels cell, which alternated the electron beam helicity at 30 Hz. A high-quality zeroth-order mica insertable (IN or OUT) half-wave plate (HWP) before the

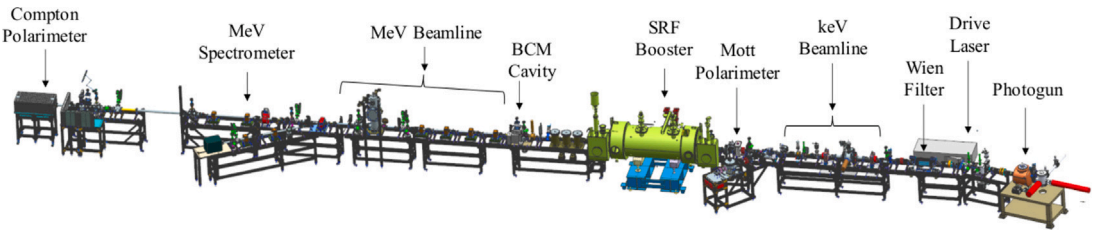

Fig. 7. The experiment at the UITF electron accelerator (beam travels right to left).

Pockels cell allowed the direction of the circular polarization, and hence the electron-beam polarization, to be reversed while leaving the Pockels cell voltages unchanged.

After the photogun, there was a Wien filter spin manipulator [41], providing crossed electric and magnetic fields normal to the beam path, that rotated the spin direction without deflecting the beam. The Wien filter was only used to set the spin direction in the vertical plane for Mott scattering polarimetry.

Solenoid magnets were used to focus and transport the electrons along the 180 keV beam line. Downstream of the Wien filter, the solenoids consisted of two coils wired with opposite polarity to give zero field integral and therefore net-zero spin rotation while providing the desired beam focusing. The two solenoids in the Mott polarimeter line are the exception. They were conventional single-coil solenoids used to both focus and purposely rotate the spin about the beam axis for Mott polarimeter calibration purposes.

A 1497 MHz normal-conducting buncher cavity compressed 60 ps bunches to a few picoseconds. The electron bunches were then accelerated to 10 MeV using the SRF cryomodule referred to as the booster. The beam energy was measured to within 5% using a spectrometer beam line with a calibrated dipole. Beyond the booster, the electron beam was transported about 5 m to the Compton transmission polarimeter using a quadrupole-magnet matching section that sets the beam size and divergence at the radiator.

There was an RF cavity beam current monitor (BCM) in the MeV beamline that provided non-invasive measurement of the delivered beam current, and more importantly, it provided a measurement of the helicity-correlated charge asymmetry that might be present on the beam. Helicity-correlated charge asymmetry can be of the order a few percent when using strained-superlattice GaAs-based photocathodes [23] due to their inherent quantum-efficiency (QE) anisotropy [42]. Unless properly minimized, helicity-correlated charge asymmetry could easily mask the Compton transmission asymmetry measured at the polarimeter. This experiment, however, utilized bulk GaAs, which does not exhibit QE anisotropy; therefore, the helicity-correlated charge asymmetry was always consistent with zero as verified by BCM measurements throughout the experiment.

The polarimeter (see Fig. 8) is preceded by diagnostic elements such as a scanning-wire beam profiler and a pair of stripline beam position monitors used to measure/set the electron-beam position and trajectory at the radiator. An insertable Faraday cup was used to measure the beam current reaching the radiator and to compare with measurements from the BCM. The radiator, which was attached to a ceramic insulator, provided a relative measurement of the current. Downstream of the radiator, the Compton transmission polarimeter components (collimator, magnet, detector) were mounted on rails and aligned concentrically to their desired positions. A lead hut 4 inches thick enclosed the radiator and polarimeter assembly, and the detector was purged with dry nitrogen to minimize water absorption by the BGO.

4. Compton polarimeter data acquisition system

The data acquisition system consisted of two parts: a Helicity Generator Board that provides signals used to orient the beam helicity, and an Ethernet Flash Analog-to-Digital Converter (EFADC) that was used to take the signals from both the Helicity Generator Board and the beam-line instruments (BCM, polarimeter PMT) and digitize them for analysis.

The Helicity Generator Board is a versatile VME-based Advanced Programmable Logic Generator [23] with vast capability and is also used at the 11 GeV accelerator (CEBAF) at Jefferson Lab. As illustrated in Fig. 9, only three signals from this board were used for this experiment. The Helicity Flip signal was used to flip voltage at the Pockels cell – and hence the electron beam helicity – every 33 830 μs. This time interval is called the *helicity window*. Helicity windows were chosen to vary in a quartet pattern as + − −+ or − + +−, with the first window selected using a pseudo-random generator. The symbols + and − indicate the polarity of the high voltage applied to the Pockels cell, either +2.5 kV or −2.5 kV. The second signal (*Delayed Helicity*) is the same as the first signal but generated by the board following an 8-window delay so the data acquisition system has no knowledge of real-time helicity. Delayed helicity ensures that data is not corrupted by false asymmetries that can arise from ground loops or helicity cross talk. The third signal (*T_Settle*) marks the start of each helicity window. This signal was used in the analysis to veto the data taken during the transition between voltage states of the Pockels cell (500 μs), allowing for the voltage – and beam polarization – to settle. Only data obtained during the stable period of 33 330 μs was used in the analysis.

The EFADC is a 250 MS/s (million samples/second) 12-bit ADC that is used to sample the input signals, in a manner similar to a digital oscilloscope. It has 16 input channels: only five channels were used to collect data during the commissioning of the Compton transmission polarimeter. Two input signals come from the helicity generator board as described above. The third input comes from the digital receiver of the BCM, which, as described above, serves as a non-invasive real-time current monitor. The fourth signal comes from the Compton transmission polarimeter, specifically the PMT used to measure the photon transmission through the analyzing magnet. The signal from the PMT was amplified and converted to voltage using a current-to-voltage low-noise pre-amplifier with a gain of 4 MΩ. For each trigger, samples over 2.04 μs were collected every 4 ns. More details about the preamp can be found in Ref. [43]. The final signal is a trigger signal used to initiate the collection of data. The detector signal can be used as the trigger; however, here a signal generator was used to produce a 78.125 kHz signal to mimic the expected beam structure at BNL.

5. Data reduction

Extracting information from raw data files requires deconstructing the data based on the structure of the EFADC signals. After the data passes through the EFADC, the spectra have a form as shown in Fig. 10.

The spectral mean location is the number of integrated channels between the average of the signal and the pedestal. Meaningful asymmetries are produced from the raw spectra by accounting for the helicity pattern, HWP status, and any chosen reporting delay. In this case, a quartet helicity with an 8-window (2-quartet) reporting delay was chosen. After adjusting for the delay, any clearly saturated events are removed from the data. Saturated events where the voltage exceeds the equipment parameters do not reflect intended physics. These events

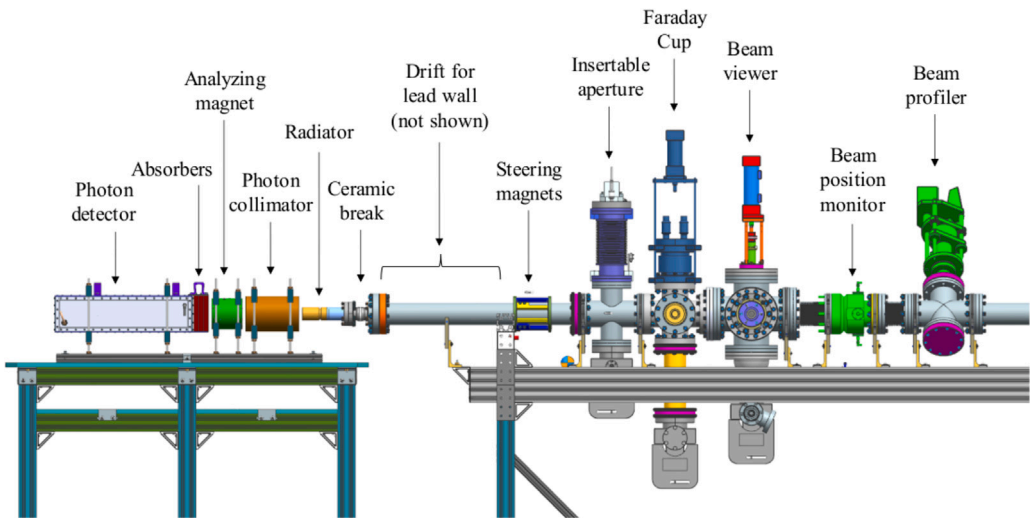

Fig. 8. The Compton transmission polarimeter and electron beam diagnostics. The elements are described in the text. A lead hut (not shown) enclosed the radiator and polarimeter assembly. This experiment did not utilize the scanning aperture.

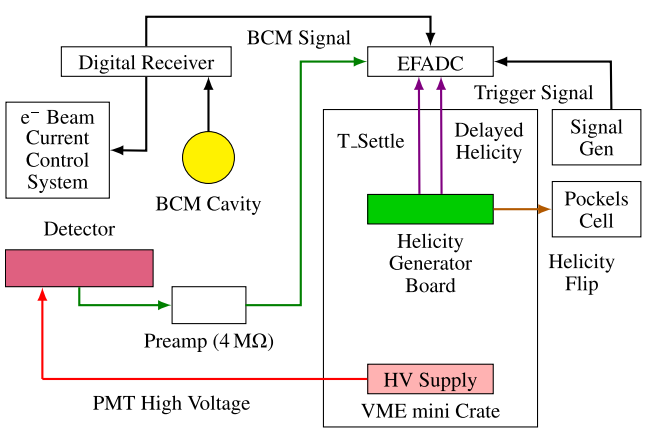

Fig. 9. A schematic of the UITF Compton polarimeter data acquisition system.

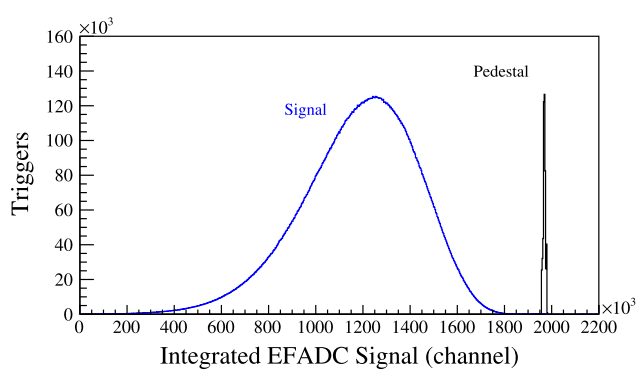

Fig. 10. The raw PMT spectrum for a calibration run at 5 MeV. The mean location is defined to be the distance from the average of this pulse to the pedestal. The pedestal is found by running the detector with no beam. This spectrum will be sorted to produce asymmetries.

are typically caused by external sources such as cosmic rays. At design parameters, the number of saturated events is multiple orders of magnitude less than the number of total events; therefore, simply removing these events from the raw spectra is a satisfactory method.

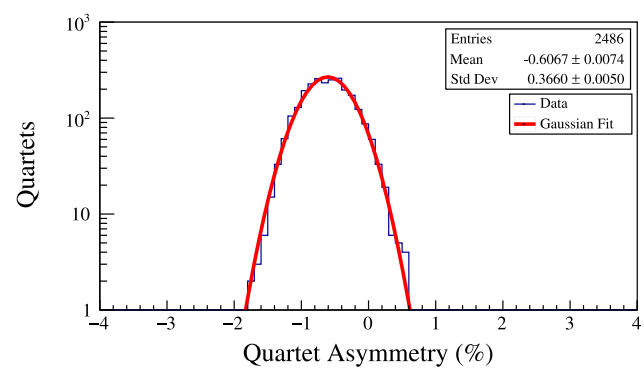

Fig. 11. Binned asymmetries with reported statistics for a calibration run at 5 MeV. The mean of these histograms will be used in the analysis.

For a signal void of saturated events, the asymmetry for a single quartet is calculated by

$$\mathrm{Asym}^{\pm}_{\mathrm{Quartet}} = \frac{\pm(w_1 + w_4) \mp (w_2 + w_3)}{w_1 + w_2 + w_3 + w_4}, \tag{15}$$

where the $\pm$ corresponds to the helicity of the first quartet window and w_i is the sum of integrated channels in the corresponding quartet window i. The resulting quartet asymmetries are binned appropriately to produce a histogram as shown in Fig. 11 for the same example run as Fig. 10.

A run asymmetry is measured for both the PMT (A_{PMT}) and BCM (A_{BCM}) signals using the histogram mean. Further analysis requires correction for any false asymmetries. One main source of false asymmetries is the HV system of the Pockels cell that was not isolated from the laser table and beamline electrical ground. This correction is accomplished by subtracting the (false) asymmetry observed when the magnet is degaussed and powered off. These false asymmetries can be denoted $A^{\mathrm{false}}_{\mathrm{PMT}}$ (PMT) and $A^{\mathrm{false}}_{\mathrm{BCM}}$ (BCM). Corrected asymmetries are defined "detector" (A_D) and "charge" (A_Q) for the PMT and BCM, respectively. The Compton asymmetry, A_E, is the difference in the detector and charge asymmetries.

$$A_D = A_{\mathrm{PMT}} - A^{\mathrm{false}}_{\mathrm{PMT}} \tag{16}$$

$$A_Q = A_{\mathrm{BCM}} - A^{\mathrm{false}}_{\mathrm{BCM}} \tag{17}$$

$$A_E = A_D - A_Q. \tag{18}$$

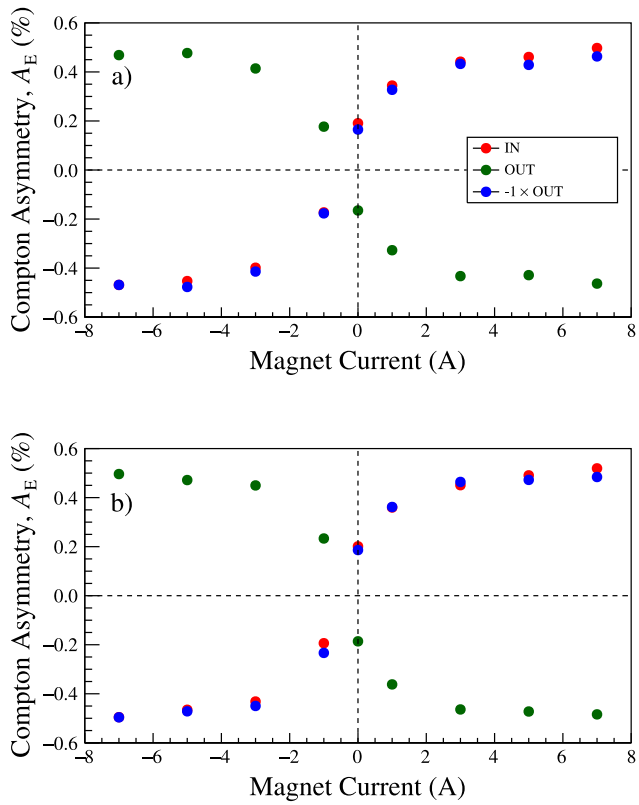

Fig. 12. (a) Compton asymmetry as a function of magnet current (A) at 5 MeV for HWP IN, OUT, and OUT × −1. (b) S-Curve repeated for incident energy of 7 MeV.

To more easily observe the underlying physics with a varied beam current, magnet current, beam size, and beam position (at the radiator), the calculated Compton asymmetries were assigned positive values, accomplished by multiplying HWP OUT results by −1.

6. Asymmetry measurements and compton analyzing power

A polarized electron beam was delivered to the radiator, and the Compton asymmetry was measured versus solenoid current to determine the best operating conditions of the magnet. Figs. 12a (5 MeV) and 12b (7 MeV) show the Compton asymmetry saturates for solenoid current above 4 A, suggesting the core is sufficiently saturated. Therefore, a magnet operating current of ±5 A was chosen for measuring the polarization. Next, a 6 nA beam was used for a sequence of calibration runs where the magnet current was reversed between ±5 A in conjunction with HWP reversals to cover all possible polarization configurations. The Compton asymmetry and effective analyzing powers were determined for 5 MeV and 7 MeV respectively (see Table 1), normalized to the Mott measured polarization of the electron beam. Electrical pickup from the Pockels Cell HV driver was the main source of the false asymmetries. The HV driver was not electrically isolated during the experiment and the real-time helicity signal (Helicity Flip) was broadcast to the experimental equipment.

7. GEANT4 simulations

A model of the polarimeter was created using GEANT4 [18–20] to predict polarimeter performance. The model includes the radiator, collimator, analyzing magnet, absorbers, and the BGO scintillator. Fig. 13 shows the electron-beam shower before and after the collimator (see Fig. 8) for the case of 2.5×10^9 mono-energetic incident electrons at 5 MeV. This number of incident electrons was selected in order to

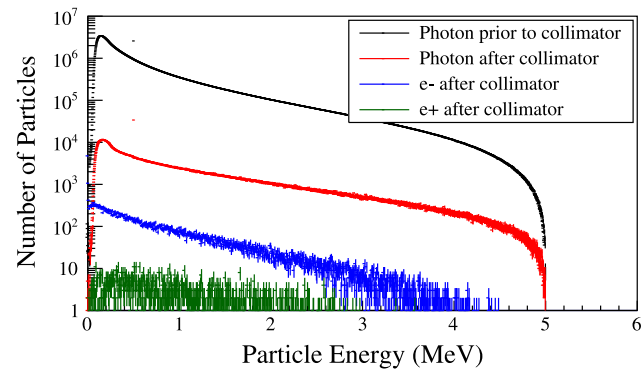

Fig. 13. Simulated bremsstrahlung photons, electrons, and positrons from GEANT4 when unpolarized mono-energetic electron beams with 2.5×10^9 electrons at 5 MeV.

generate sufficient statistics. Here, the total number of photons in the shower is greatly reduced following the collimator.

Next, the electron beam was polarized, either parallel (+) or anti-parallel (−) to the magnet polarization, for the purpose of producing asymmetry results inside the detector. The electron beam and target polarizations are chosen as 100%, and the polarized electromagnetic physics package of GEANT4 was then used to simulate the detector response. Fig. 14a shows the detector energy deposit by counting the number of photons that deposit their energies for each electron beam polarization. Then, Fig. 14b shows the asymmetry as a function of this energy, calculated as follows:

$$A(U_i) = \frac{N_i^+ - N_i^-}{N_i^+ + N_i^-}, \tag{19}$$

where $N_i^\pm$ corresponds to the number of photons with energy deposition U_i for a given direction of longitudinal polarization. In Fig. 14b, the magnitude of the asymmetry grows because the photon polarization is larger at higher energy. Statistical error is less at lower energy because lower-energy photons are more abundant as shown in Fig. 13.

Observing an asymmetry of the deposited photon energy by experiment is not feasible due to the large number of photons (with various energies) contributing to the detector signal causing the data rate to be too high to resolve individual events. Experimentally, a signal is integrated over a full helicity window, capturing the sum of energies for a large number of photons. The asymmetry can then be formulated as an energy-weighted count asymmetry following the expression

$$A_S = \frac{\sum_i A(U_i)E_i}{\sum_i E_i}, \tag{20}$$

where

$$E_i = E_i^+ + E_i^- = U_i(N_i^+ + N_i^-) \tag{21}$$

is the helicity-independent energy deposit per energy bin i. For comparison with experiment, the results generated with 100% target polarization are multiplied by the (8.020 ± 0.018)% theoretical maximum iron electron polarization [32] to produce a simulated effective analyzing power. This process is repeated for 3, 7, and 9 MeV to observe the response to different beam energies for the simulated effective analyzing power. This behavior is shown in Fig. 15 and recorded in Table 1.

8. Discussion

8.1. PMT and BCM linearity and threshold effects

Prior to performing the aforementioned calibration runs, the systematics of the Compton polarimeter were studied to find the operational beam current with limited saturation. Here, the UITF beam current was varied from 1 nA to 10 nA, and the spectral mean location,

Table 1
Experimental and simulated results of the Compton transmission polarimeter. False asymmetries reported are the average of HWP IN and OUT states. Simulated results assumed a 100% beam polarization and will be discussed in detail in Section 7.

	Measured					Simulated		
Beam Energy (MeV)	PMT False Asymmetry $A^{\text{false}}_{\text{PMT}}$ (%)	BCM False Asymmetry $A^{\text{false}}_{\text{BCM}}$ (%)	Compton Asymmetry A_E (%)	Experimental Beam Polarization (%)	Effective Analyzing Power $\mathcal{A}_{\text{eff}}$ (%)	Compton Asymmetry A_S (%)	Target Polarization (%)	Effective Analyzing Power (%)
3						14.08 ± 0.69	8.020 ± 0.018	1.12 ± 0.06
5	0.107 ± 0.004	0.123 ± 0.002	0.451 ± 0.004	37.7 ± 2.3	1.20 ± 0.07	16.12 ± 0.27	8.020 ± 0.018	1.29 ± 0.02
7	0.119 ± 0.003	0.133 ± 0.004	0.481 ± 0.007	37.7 ± 2.3	1.28 ± 0.08	15.50 ± 0.15	8.020 ± 0.018	1.24 ± 0.01
9						13.26 ± 0.10	8.020 ± 0.018	1.06 ± 0.01

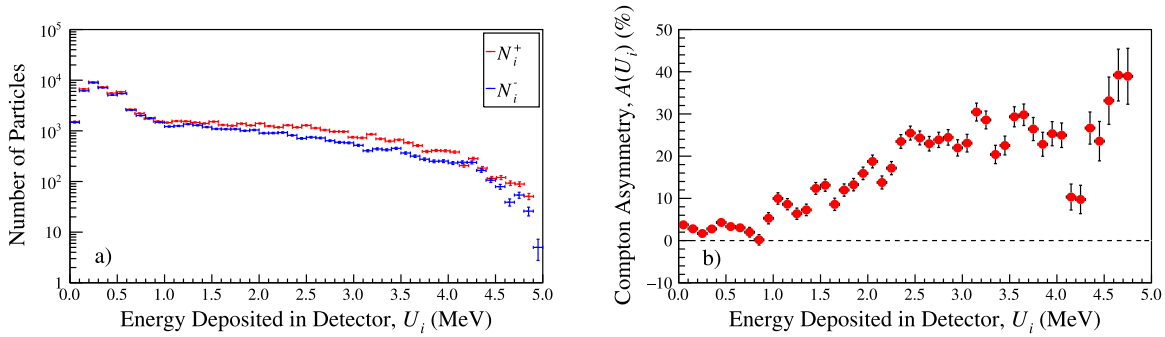

Fig. 14. (a) Simulated BGO energy deposition spectra for parallel and anti-parallel polarized electron beams with 2.5×10^9 electrons at 5 MeV. (b) Asymmetry for each photon energy deposit at 5 MeV and a beam size of 0.22 mm assuming 100% iron core polarization.

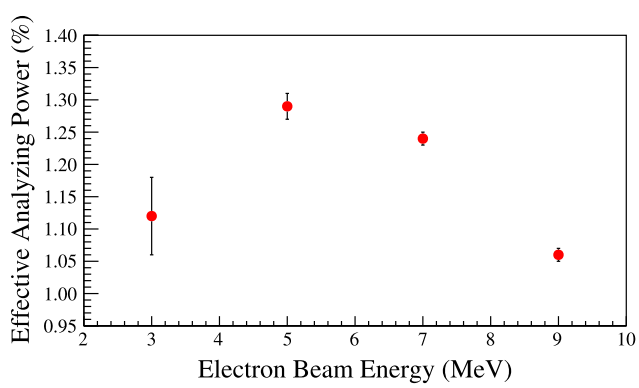

Fig. 15. Simulated effective analyzing power as a function of incident electron beam energy. Here, the target polarization is set to (8.020 ± 0.018)%.

asymmetry, and the asymmetry width, σ, were recorded for the detector and charge signals. As mentioned above, the HWP OUT results are multiplied by −1 to compare between HWP states.

The pulse migrates away from the pedestal location as increased particle counts in higher beam currents generate more events and thus larger signals. The signal magnitude (spectral mean location) should have a linear relationship with beam current due to linear growth in bremsstrahlung generation with increased beam current. This linearity is checked in order to ensure the method of calculating asymmetries is applicable. Figs. 16a and 16d show the correspondence between the mean location and beam current for both detector and charge signals at 5 MeV and 7 MeV. Here, no evidence of saturation is found for the signal magnitude within the chosen range.

Asymmetry should have no beam-current dependence, and the charge asymmetry should be consistent with zero (for bulk GaAs). Increased beam current does not alter the polarization on which asymmetry is dependent. Asymmetry is shown as a function of beam current in Figs. 16b and 16e. These results show a detector asymmetry of roughly 0.45% and a charge asymmetry that is consistent with zero. Low-current results exhibit pedestal interference and as such apply a lower bound on the calibration range of roughly 2 nA.

Raising the electron-beam current increases the photon count reaching the detector; thus, the asymmetry width decreases due to better statistics. Proper statistical behavior requires σ to be inversely proportional to the square root of the beam current. Asymmetry width versus beam current is shown in Figs. 16c and 16f for the detector and charge signals, respectively. The same low-current limit appears here with additional high-current saturation effects. These saturated results put an upper limit on the calibration range of around 7 nA.

In order to avoid saturation, the Compton transmission polarimeter was calibrated at 6 nA. This beam current maximizes statistics while demonstrating proper statistical behavior of the spectral mean location, asymmetry, and asymmetry width. Additional absorbers would enable operation at higher current.

8.2. Target polarization

The results shown in Fig. 15 use a target polarization of (8.020 ± 0.018)% to report a simulated effective analyzing power. However, the experimental results can also be used to calculate a target polarization that reflects real results. Here, the experimental asymmetries ((0.451 ± 0.004)% and (0.481 ± 0.007)% at 5 MeV and 7 MeV) and the known beam polarization (37.7 ± 2.3)% can be introduced. The iron core polarization can be calculated by dividing the experimental asymmetries by the beam polarization and simulated analyzing power (prior to the introduction of any target polarization) in accordance with Eq. (14) and then averaging between the two energies (5 MeV and 7 MeV).

The resulting core polarization is (7.84 ± 0.35)% and is consistent with the theoretical limit of (8.020 ± 0.018)% used in the analysis [32]. However, this result assumes that the core is uniformly polarized, which is a major oversimplification (see Fig. 4). This result shows that the choice to use the theoretical maximum provides a good representation of polarimeter behavior. If the polarization profile were well known, further information could be extracted.

8.3. Compton asymmetry dependence on electron beam position

The position of the electron beam at the radiator for all of the Compton asymmetry studies was centered with the axis of the collimator. This was determined using a graticulated X-ray fluorescence card

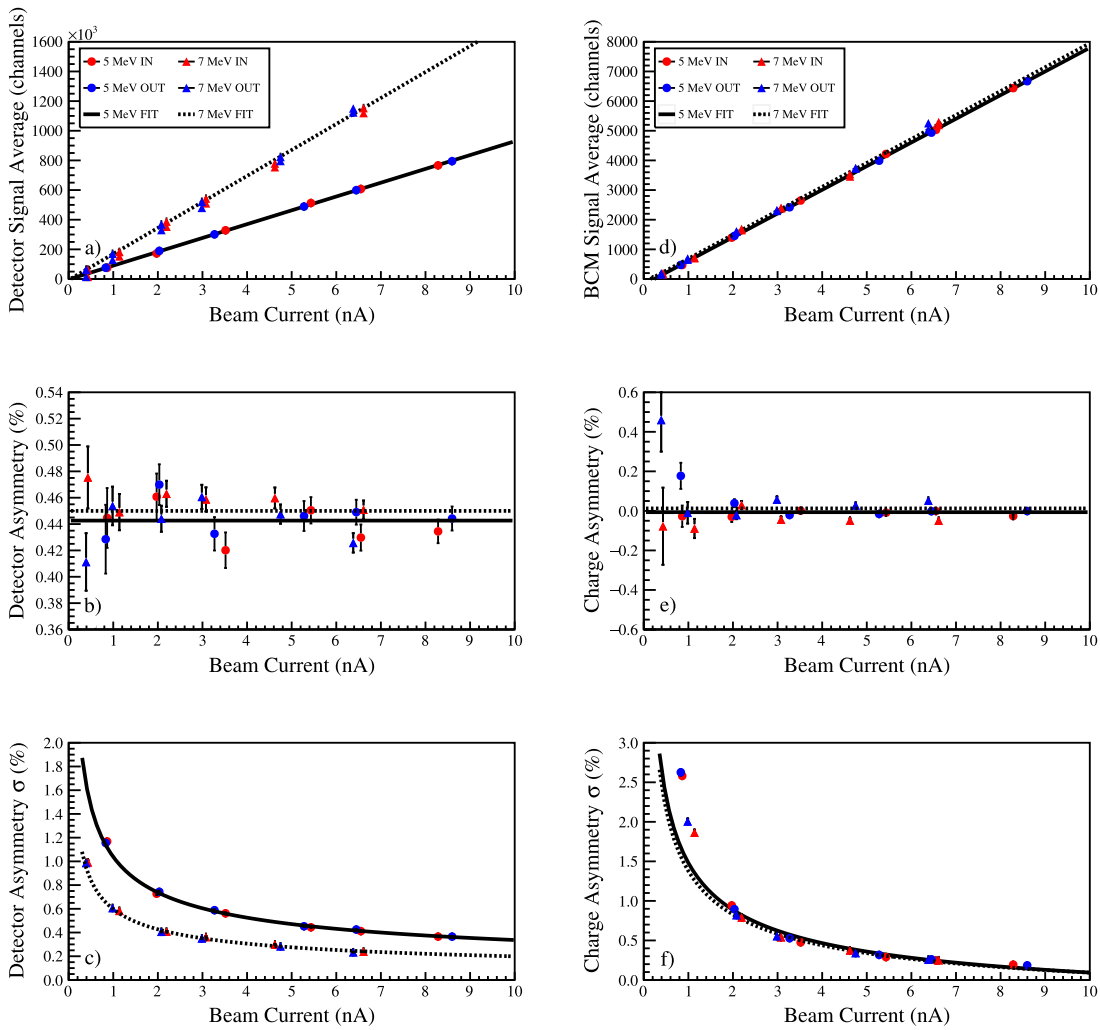

Fig. 16. LEFT: Detector signal properties as a function of beam current. RIGHT: Charge signal properties as a function of beam current. Measurements are made in both HWP states (IN and OUT). Data (7 MeV 9 nA) has been removed due to saturation (a) Detector mean location. The definition of the mean location is described in Fig. 10. (b) Detector asymmetry. (c) Detector asymmetry width, σ. (d) Charge mean location. (e) Charge asymmetry. (f) Charge asymmetry width, σ.

whose origin was aligned to be coincident with the collimator axis. While the electron beam was scanned horizontally and vertically at the radiator the photon beam produced at the X-ray card was measured and analyzed with video analysis software. This scan was used to finalize the nominal electron beam orbit which resulted in a photon beam centered on the collimator.

Later, once the Compton polarimeter was functioning and calibrated, a dedicated study was performed to measure the sensitivity of the Compton asymmetry to the electron beam position at the radiator. The electron beam (5 MeV and 1.55 mm radius) was moved horizontally and vertically, and the Compton asymmetries were measured. For each measurement beam position monitors were used to precisely measure the relative displacement from the nominally centered position.

Fig. 17a summarizes five Compton asymmetries measured in the study; a Compton asymmetry for a nominal run (with the collimator aperture for scale) is shown along with these five measurements comprising the "cross" formed from horizontal and vertical scans. It was recognized afterwards that a retune of the accelerator had caused the beam orbit to change, displacing the cross by about 4.3 mm in x and 8 mm in y.

Although unintentional and further from the collimator axis, these Compton asymmetry measurements are perfectly useful. Shown in Fig. 17b are again the same measurements, but now plotted as a function of radius from the collimator axis. In addition, simulated Compton asymmetries performed using the GEANT4 model (5 MeV and 1.55 mm) are shown for comparison. Due to the large uncertainty of the absolute beam position in this data set, the measured points do not align with the simulation; however, the slope is reproduced well, suggesting the collimator behaves as modeled.

In summary, we intended to measure the sensitivity of the Compton asymmetry for smaller radii (< 4 mm) but measured them for larger radii (> 6 mm). Unfortunately, we do not have measurements at radii from $r = 2$ mm to $r = 6$ mm predicted by GEANT4 simulations. However, the overall agreement of model with measurement suggests the Compton analyzing power should be relatively insensitive when all of the electron beam falls within a radius of 4 mm, independent of the beam size.

9. Conclusion

We described a Compton transmission electron polarimeter constructed for the purpose of measuring the longitudinally polarized electron beam to be generated via photoemission from GaAs in an SRF photogun at Brookhaven National Lab. Key components of the polarimeter (bremsstrahlung radiator, polarized target, photon detector), the data acquisition system and an experiment performed at the Upgraded Injector Test Facility at Jefferson Lab to calibrate the polarimeter with a known spin-polarized electron beam were discussed.

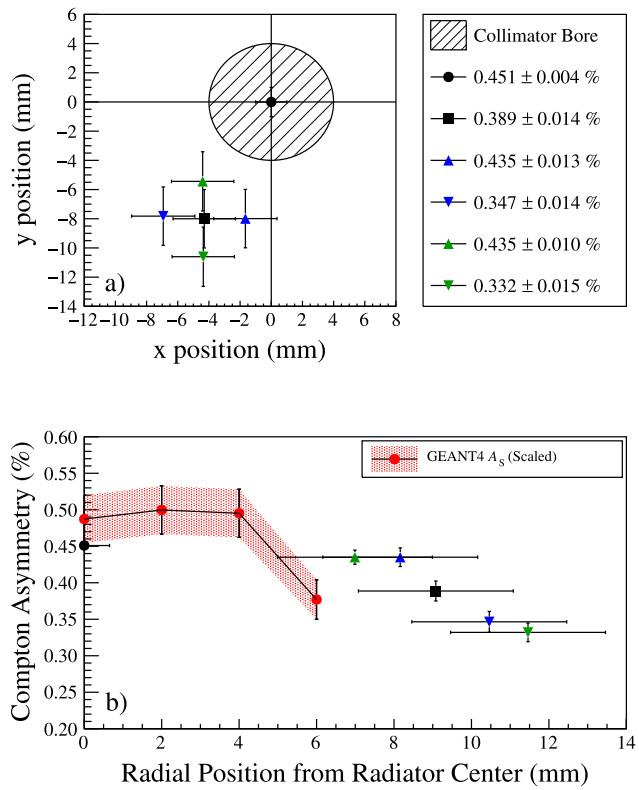

Fig. 17. (a) shows the Compton asymmetry for the electron beam nominally centered with the collimator compared with those when the electron beam was scanned in a "cross" centered about 9 mm from the collimator axis. (b) The same six measurements, but now plotted as a function of radius from the collimator axis, alongside simulated Compton asymmetries computed using the GEANT4 model (5 MeV and 1.55 mm) for comparison. The simulated beam polarization is (37.7 ± 2.3)%, and the simulated target polarization is (8.020 ± 0.018)%.

We report systematic studies of the polarimeter performance, supporting GEANT4 simulations useful to predict polarimeter behavior, and an effective analyzing power of 1.20% (5 MeV) and 1.28% (7 MeV).

CRediT authorship contribution statement

G. Blume: Writing – original draft, Writing – review & editing, Methodology, Software, Validation, Formal Analysis, Investigation, Data Curation, Visualization. **M. Bruker:** Writing – original draft, Writing – review & editing, Investigation. **C. Cuevas:** Software, Resources. **H. Dong:** Software, Resources. **Benjamin Fernandes Neres:** Methodology. **P. Ghoshal:** Visualization, Resources. **S. Gopinath:** Writing – original draft, Visualization, Resources. **J. Grames:** Writing – original draft, Writing – review & editing, Conceptualization, Software, Validation, Investigation, Resources, Supervision, Project administration, Funding acquisition. **S. Gregory:** Methodology, Resources. **G. Hays:** Methodology, Resources. **C. Le Galliard:** Resources. **S. Marsillac:** Writing – original draft, Writing – review & editing, Validation. **B. Moffit:** Software, Resources. **Thi Nguyen Trung:** Resources. **M. Poelker:** Writing – review & editing, Investigation. **R. Suleiman:** Writing – original draft, Writing – review & editing, Conceptualization, Validation, Investigation, Resources, Supervision, Project administration, Funding acquisition. **E. Voutier:** Writing – original draft, Writing – review & editing, Conceptualization, Validation, Investigation, Resources. **S. Zhang:** Writing – original draft, Writing – review & editing, Investigation.

Declaration of competing interest

The authors declare that they have no known competing financial interests or personal relationships that could have appeared to influence the work reported in this paper.

Data availability

Data will be made available on request.

Acknowledgments

This material is based upon work supported by the U.S. Department of Energy, Office of Science, Office of Nuclear Physics, contract DE-AC05-06OR23177 and contract No. DE-SC0021039 under which Jefferson Science Associates, LLC operates JLab. It is part of a project that has received funding from the European Union's Horizon 2020 research and innovation program under agreement STRONG - 2020 - No 824093. This material is based upon work funded by U.S. Department of Energy FOA Number LAB 20-2310.

Appendix. UITF Mott polarimeter

A.1. Methodology

Mott-scattering polarimetry relies on electrons elastically scattered by the Coulomb field of heavy nuclei [44] with an integrated cross section [45]

$$\sigma(\theta,\phi) = I(\theta)[1 + S(\theta)\vec{P}\cdot\hat{n}], \tag{A.1}$$

where the unpolarized cross section is

$$I(\theta) = \frac{Z^2e^4}{4m^2\beta^4c^4\sin^2(\theta/2)}[1-\beta^2\sin^2(\theta/2)](1-\beta^2), \tag{A.2}$$

and $\vec{P}$ is the polarization vector, $\hat{n} = \frac{\vec{k}\times\vec{k'}}{|\vec{k}\times\vec{k'}|}$ is the unit vector perpendicular to the scattering plane determined by the electron momentum before ($\hbar\vec{k}$) and after ($\hbar\vec{k'}$) scattering, and $S(\theta)$ is the Sherman Function [46]. Fig. A.18 shows the Sherman Function [47,48] as a function of scattering angle for 180 keV electrons off a gold atom.

A vertically polarized electron beam incident on a heavy-Z target (like gold) will generate a sizable left–right asymmetry [45].

The usual way to use a Mott polarimeter is to measure the scattering asymmetry for several foil thicknesses and extrapolate to find the asymmetry for a hypothetical zero-thickness foil, or single atom. With the experimentally determined single-atom scattering asymmetry measured, and the single-atom Sherman function predicted by theory, the beam polarization can be assigned. In this experiment, four different

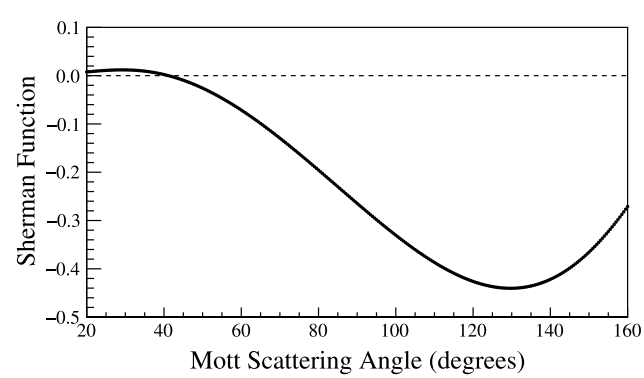

Fig. A.18. The Sherman Function as a function of angle at 180 keV.

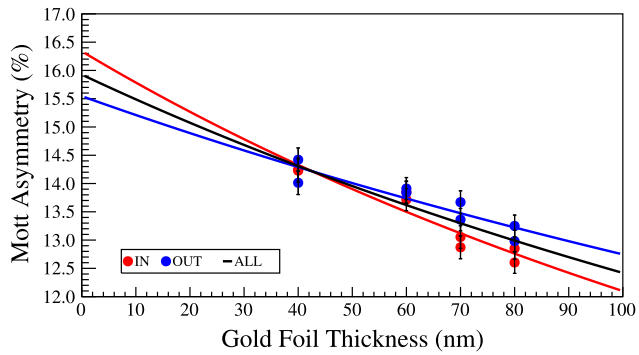

Fig. A.19. Zero-thickness asymmetry extrapolation for the Mott polarimeter for 180 keV electrons emitted from bulk GaAs. The insertable (IN or OUT) HWP used previously was applied here to reverse the electron-beam polarization. Similar to the analysis above, the OUT results are multiplied by –1.

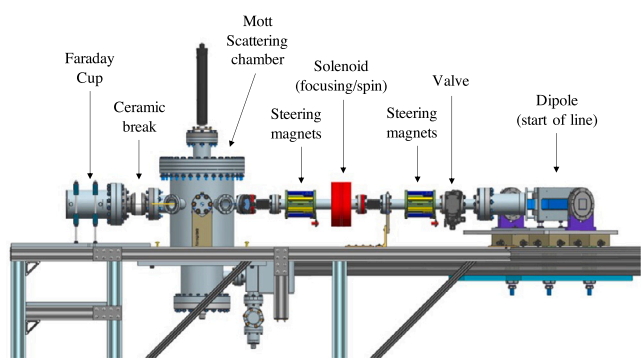

Fig. A.20. Mott polarimeter beamline (beam travels from right to left).

gold foil thicknesses were used to extrapolate to zero foil thickness. The data is plotted in Fig. A.19.

Data was fit using the functional form [49]

$$A = \frac{A_E(t=0)}{1.0 + \beta t}, \tag{A.3}$$

where $A_E(t = 0)$ is the zero-thickness asymmetry and β characterizes the dependence of the measured asymmetry on target thickness. Here, the extrapolated zero-thickness asymmetry is $(15.9 \pm 0.5\ (\text{stat}) \pm 0.9\ (\text{syst}))$ % and $\beta = (0.0028 \pm 0.0004)$/nm. Combining this with Eq. (14), beam polarization is given by

$$P_e^1 = \frac{A_E(t=0)}{S(180\,\text{keV}, 120°)} = \frac{(15.9 \pm 1.0)\%}{(0.423 \pm 0.003)\%} = (37.7 \pm 2.3)\%. \tag{A.4}$$

A.2. Hardware

The Mott polarimeter is located in the spectrometer beamline of the keV section of the UITF accelerator (as shown in Fig. 7). A Wien-filter spin manipulator is used to orient the spin direction in the vertical plane. A solenoid magnet composed of two coils that are independently powered provides beam focusing and can be used to rotate the transverse component of the spin-polarization for systematic studies, if desired. Steering magnets set the beam orbit through the polarimeter and to the downstream Faraday cup used to measure beam current (see details in Fig. A.20).

The Mott polarimeter vacuum chamber (shown in Fig. A.21) includes a stepper-motor-controlled target ladder, two pairs of detectors for monitoring forward and back-scattered electrons, and vacuum pumps (non-evaporable getter (NEG) and ion pump) to achieve ultra-high vacuum compatible with the requirements of the spin-polarized electron source situated approximately 5 m away.

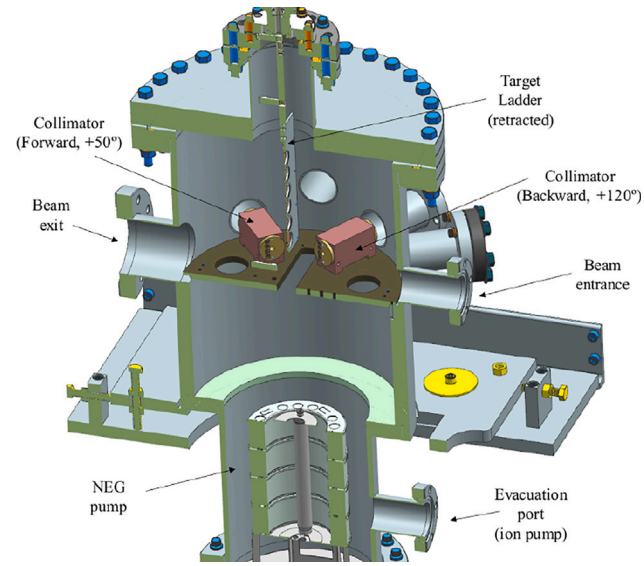

Fig. A.21. The Mott polarimeter scattering chamber. The forward (50 degrees) detectors were not used in this experiment.

There are a total of six target-ladder positions, four of them for gold foils (40 nm, 60 nm, 70 nm, and 80 nm thicknesses [50]), one for a beam viewer and one for a through-hole. The through-hole is included to detect background generated by beam halo striking the frame of the ladder, but here no background was observed. The target ladder can also be fully retracted from the beam path.

Electrons scatter from the gold foil targets in all directions. Detectors are placed where the Sherman function is a maximum (± 120 degrees) to measure the Mott-scattering asymmetry, and where the Sherman function is very close to zero (± 50 degrees) to study false asymmetries (see Fig. A.18).

In front of each detector, there is an acceptance-defining aperture (2 mm diameter). The apertures were precisely placed on an alignment plate welded to the inside of the vacuum chamber. After scattering from the gold foil and passing through the collimators, the electrons reach silicon surface-barrier detectors within a solid angle of 1.7 msr. The detectors are biased at 180 V and have a 50 mm^2 active area and a 50 µm depletion depth to improve signal-to-noise ratio. The detectors are bakeable up to 200 °C. Measurements were done with beam currents from 1 nA to 5 nA.

Electrons reaching the silicon surface-barrier detectors produce a signal proportional to its energy, which is connected to a low-noise, fast-rise-time, charge-sensitive preamplifier with a 6-inch cable through a BNC vacuum feed-through. The signal is then routed outside of the beam enclosure to an amplifier and timing single-channel analyzer (SCA). The amplified energy output is then connected to a flash Analog-to-Digital Converter (fADC) in a VXS crate and is read out by a Linux single board computer (SBC). The fADC used here is a 125 MS/s (million samples/second) 12-bit ADC that is used to sample the input signals similar to a digital oscilloscope. Fig. A.22 shows a schematic of the data acquisition system. The helicity signals used with the Mott polarimeter are similar to those described in the main paper when describing the Compton transmission polarimeter.

The Mott trigger is a logic-OR of the left and right detector signals and is connected to a trigger interface distribution (TID) board. For each trigger, samples during 4 µs were collected every 4 ns. The fADC output consists of 500 samples as shown in Fig. A.23. The 500 fADC samples per event are summed to calculate the energy of the detected electron.

Fig. A.24 shows the energy spectra for the Right and Left detectors. For each asymmetry measurement, the Right and Left energy spectra

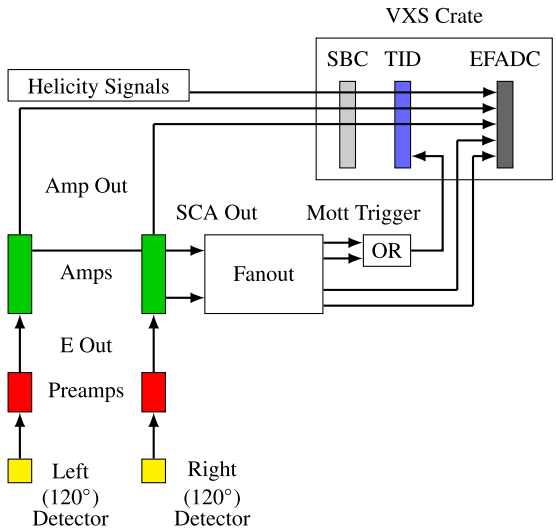

Fig. A.22. A schematic of the UITF Mott data acquisition system.

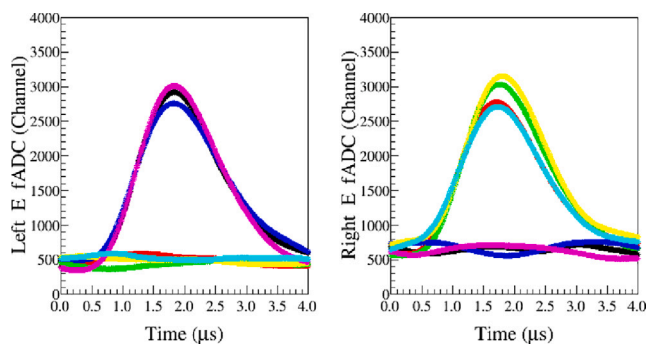

Fig. A.23. Mott detector signals showing few events. When an electron hits one of the detectors and deposits energy, the other detector almost always reads a pedestal since the scattering rate is so low.

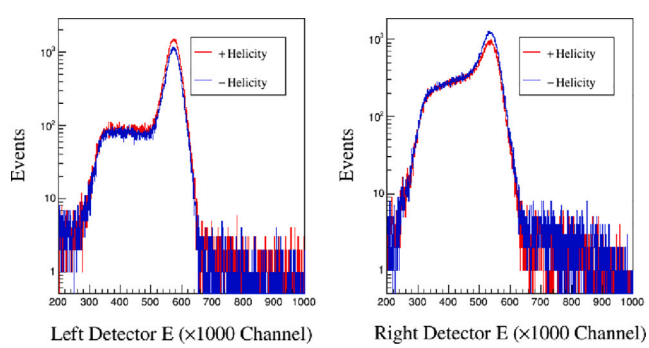

Fig. A.24. Number of electrons with positive (red plot) and negative helicity (blue plot) with a certain energy for the target of 40 nm thickness. The left and right plots represent the Left and Right detectors, respectively.

were sorted per helicity. The elastic peak was fitted with a Gaussian, and the number of elastic electrons per detector and per helicity was determined by selecting events in the range -0.5σ to 2.0σ where σ is the standard deviation of the Gaussian fit. The Right–Left asymmetry was then calculated using the cross-ratio method [51].

References

[1] E. Wang, O. Rahman, J. Skaritka, W. Liu, J. Biswas, C. Degen, P. Inacker, R. Lambiase, M. Paniccia, High voltage dc gun for high intensity polarized electron source, Phys. Rev. Accel. Beams 25 (2022) 033401, http://dx.doi.org/10.1103/PhysRevAccelBeams.25.033401, URL https://link.aps.org/doi/10.1103/PhysRevAccelBeams.25.033401.

[2] C. Hernandez-Garcia, P. Adderley, B. Bullard, J. Benesch, J. Grames, J. Gubeli, F. Hannon, J. Hansknecht, J. Jordan, R. Kazimi, G.A. Krafft, M.A. Mamun, M. Poelker, M.L. Stutzman, R. Suleiman, M. Tiefenback, Y. Wang, S. Zhang, H. Baumgart, G. Palacios-Serrano, S. Wijethunga, J. Yoskowitz, C.A. Valerio Lizarraga, R. Montoya Soto, A. Canales Ramos, Compact −300 kV dc inverted insulator photogun with biased anode and alkali-antimonide photocathode, Phys. Rev. Accel. Beams 22 (2019) 113401, http://dx.doi.org/10.1103/PhysRevAccelBeams.22.113401, URL https://link.aps.org/doi/10.1103/PhysRevAccelBeams.22.113401.

[3] J. Maxson, I. Bazarov, B. Dunham, J. Dobbins, X. Liu, K. Smolenski, Design, conditioning, and performance of a high voltage, high brightness dc photoelectron gun with variable gap, Rev. Sci. Instrum. 85 (9) (2014) http://dx.doi.org/10.1063/1.4895641, 093306.

[4] N. Nishimori, R. Nagai, S. Matsuba, R. Hajima, M. Yamamoto, Y. Honda, T. Miyajima, H. Iijima, M. Kuriki, M. Kuwahara, Experimental investigation of an optimum configuration for a high-voltage photoemission gun for operation at ≥ 500 kV, Phys. Rev. ST Accel. Beams 17 (2014) 053401, http://dx.doi.org/10.1103/PhysRevSTAB.17.053401, URL https://link.aps.org/doi/10.1103/PhysRevSTAB.17.053401.

[5] D. Conti, S. Navert, K. Bodek, W. Haeberli, S. Kistryn, J. Lang, O. Naviliat, E. Reichert, J. Sromicki, M. Steigerwald, E. Stephan, J. Zejma, Mott scattering of multi-MeV electrons from heavy nuclei, in: The Seventh International Workshop on Polarized Gas Targets and Polarized Beams, in: American Institute of Physics Conference Series, vol. 421, 1998, pp. 326–335, http://dx.doi.org/10.1063/1.55004.

[6] J. Sromicki, K. Bodek, D. Conti, S. Kistryn, J. Lang, S. Navert, O. Naviliat-Cuncic, E. Stephan, C. Sys, J. Zejma, W. Haeberli, E. Reichert, M. Steigerwald, Polarization in mott scattering of multi-MeV electrons from heavy nuclei, Phys. Rev. Lett. 82 (1999) 57–60, http://dx.doi.org/10.1103/PhysRevLett.82.57, URL https://link.aps.org/doi/10.1103/PhysRevLett.82.57.

[7] C.K. Sinclair, P.A. Adderley, B.M. Dunham, J.C. Hansknecht, P. Hartmann, M. Poelker, J.S. Price, P.M. Rutt, W.J. Schneider, M. Steigerwald, Development of a high average current polarized electron source with long cathode operational lifetime, Phys. Rev. ST Accel. Beams 10 (2007) 023501, http://dx.doi.org/10.1103/PhysRevSTAB.10.023501, URL https://link.aps.org/doi/10.1103/PhysRevSTAB.10.023501.

[8] Y.C. Chao, M. Drury, C. Hovater, A. Hutton, G.A. Krafft, M. Poelker, C. Reece, M. Tiefenback, CEBAF accelerator achievements, J. Phys. Conf. Ser. 299 (1) (2011) 012015, http://dx.doi.org/10.1088/1742-6596/299/1/012015.

[9] T. Zwart, E.C. Booth, M. Farkhondeh, W.A. Franklin, E. Ihloff, J.L. Matthews, E. Tsentalovich, W. Turchinetz, Transmission polarimetry at MIT bates, AIP Conf. Proc. 675 (1) (2003) 1011–1015, http://dx.doi.org/10.1063/1.1607286.

[10] T. Zwart, E. Booth, F. Casagrande, K. Dow, M. Farkhondeh, W. Franklin, E. Ihloff, K. Jacobs, J. Matthews, R. Milner, T. Smith, C. Tschalaer, E. Tsentalovich, W. Turchinetz, F. Wang, Polarized electrons at Bates: Source to storage ring, AIP Conf. Proc. 588 (1) (2001) 343–349, http://dx.doi.org/10.1063/1.1413178.

[11] R. Barday, K. Aulenbacher, P. Bangert, J. Enders, A. Göök, D.H. Jakubassa-Amundsen, F. Nillius, A. Surzhykov, V.A. Yerokhin, Compton transmission polarimeter for a very precise polarization measurement within a wide range of electron currents, J. Phys. Conf. Ser. 298 (1) (2011) 012022, http://dx.doi.org/10.1088/1742-6596/298/1/012022.

[12] C. Weinrich, A4 Collaboration, The transmission Compton polarimeter of the A4 experiment, in: S. Kox, D. Lhuillier, F. Maas, J. Van de Wiele (Eds.), Eur. Phys. J. A 24S2 (2005) 129–130, http://dx.doi.org/10.1140/epjad/s2005-04-030-2.

[13] J.M. Grames, C.K. Sinclair, J. Mitchell, E. Chudakov, H. Fenker, A. Freyberger, D.W. Higinbotham, M. Poelker, M. Steigerwald, M. Tiefenback, C. Cavata, S. Escoffier, F. Marie, T. Pussieux, P. Vernin, S. Danagoulian, V. Dharmawardane, R. Fatemi, K. Joo, M. Zeier, V. Gorbenko, R. Nasseripour, B. Raue, R. Suleiman, B. Zihlmann, Unique electron polarimeter analyzing power comparison and precision spin-based energy measurement, Phys. Rev. ST Accel. Beams 7 (2004) 042802, http://dx.doi.org/10.1103/PhysRevSTAB.7.042802, URL https://link.aps.org/doi/10.1103/PhysRevSTAB.7.042802.

[14] J. Magee, A. Narayan, D. Jones, R. Beminiwattha, J. Cornejo, M. Dalton, W. Deconinck, D. Dutta, D. Gaskell, J. Martin, K. Paschke, V. Tvaskis, A. Asaturyan, J. Benesch, G. Cates, B. Cavness, L.A. Dillon-Townes, G. Hays, J. Hoskins, E. Ihloff, R. Jones, P. King, S. Kowalski, L. Kurchaninov, L. Lee, A. McCreary, M. McDonald, A. Micherdzinska, A. Mkrtchyan, H. Mkrtchyan, V. Nelyubin, S. Page, W. Ramsay, P. Solvignon, D. Storey, W. Tobias, E. Urban, C. Vidal, B. Waidyawansa, P. Wang, S. Zhamkotchyan, A novel comparison of Møller and Compton electron-beam polarimeters, Phys. Lett. B 766 (2017) 339–344, http://dx.doi.org/10.1016/j.physletb.2017.01.026, URL https://www.sciencedirect.com/science/article/pii/S0370269317300333.

[15] I. Petrushina, V.N. Litvinenko, Y. Jing, J. Ma, I. Pinayev, K. Shih, G. Wang, Y.H. Wu, Z. Altinbas, J.C. Brutus, S. Belomestnykh, A. Di Lieto, P. Inacker, J. Jamilkowski, G. Mahler, M. Mapes, T. Miller, G. Narayan, M. Paniccia, T. Roser, F. Severino, J. Skaritka, L. Smart, K. Smith, V. Soria, Y. Than, J.

Tuozzolo, E. Wang, B. Xiao, T. Xin, I. Ben-Zvi, C. Boulware, T. Grimm, K. Mihara, D. Kayran, T. Rao, High-brightness continuous-wave electron beams from superconducting radio-frequency photoemission gun, Phys. Rev. Lett. 124 (2020) 244801, http://dx.doi.org/10.1103/PhysRevLett.124.244801, URL https://link.aps.org/doi/10.1103/PhysRevLett.124.244801.

[16] E. Wang, V.N. Litvinenko, I.P.M. Gaowei, J. Skaritka, S. Belomestnykh, I. Ben-Zvi, J.C. Brutus, Y. Jing, J. Biswas, J. Ma, G. Narayan, I. Petrushina, O. Rahman, T. Xin, T. Rao, F. Severino, K. Shih, K. Smith, G. Wang, Y. Wu, Long lifetime of bialkali photocathodes operating in high gradient superconducting radio frequency gun, Sci. Rep. 11 (2021) 4477, http://dx.doi.org/10.1038/s41598-021-83997-1, URL https://www.sciencedirect.com/science/article/pii/S0370269317300333.

[17] I. Petrushina, Y. Jing, V.N. Litvinenko, J. Ma, I. Pinayev, G. Wang, D. Kayran, F. Severino, G. Narayan, T. Hayes, J.C. Brutus, L. Smart, K. Decker, S. Belomestnykh, First experience with He conditioning of a superconducting rf photoinjector, Phys. Rev. Accel. Beams 25 (2022) 092001, http://dx.doi.org/10.1103/PhysRevAccelBeams.25.092001, URL https://link.aps.org/doi/10.1103/PhysRevAccelBeams.25.092001.

[18] S. Agostinelli, et al., Geant4—a simulation toolkit, Nucl. Instrum. Methods A 506 (3) (2003) 250–303, http://dx.doi.org/10.1016/S0168-9002(03)01368-8, URL https://www.sciencedirect.com/science/article/pii/S0168900203013688.

[19] J. Allison, et al., Geant4 developments and applications, IEEE Trans. Nucl. Sci. 53 (1) (2006) 270–278, http://dx.doi.org/10.1109/TNS.2006.869826.

[20] J. Allison, et al., Recent developments in Geant4, Nucl. Instrum. Methods A 835 (2016) 186–225, http://dx.doi.org/10.1016/j.nima.2016.06.125, URL https://www.sciencedirect.com/science/article/pii/S0168900216306957.

[21] D. Abbott, P. Adderley, A. Adeyemi, P. Aguilera, M. Ali, H. Areti, M. Baylac, J. Benesch, G. Bosson, B. Cade, A. Camsonne, L.S. Cardman, J. Clark, P. Cole, S. Covert, C. Cuevas, O. Dadoun, D. Dale, H. Dong, J. Dumas, E. Fanchini, T. Forest, E. Forman, A. Freyberger, E. Froidefond, S. Golge, J. Grames, P. Guèye, J. Hansknecht, P. Harrell, J. Hoskins, C. Hyde, B. Josey, R. Kazimi, Y. Kim, D. Machie, K. Mahoney, R. Mammei, M. Marton, J. McCarter, M. McCaughan, M. McHugh, D. McNulty, K.E. Mesick, T. Michaelides, R. Michaels, B. Moffit, D. Moser, C. Muñoz Camacho, J.-F. Muraz, A. Opper, M. Poelker, J.-S. Réal, L. Richardson, S. Setiniyaz, M. Stutzman, R. Suleiman, C. Tennant, C. Tsai, D. Turner, M. Ungaro, A. Variola, E. Voutier, Y. Wang, Y. Zhang, PEPPo Collaboration Collaboration, Production of highly polarized positrons using polarized electrons at MeV energies, Phys. Rev. Lett. 116 (2016) 214801, http://dx.doi.org/10.1103/PhysRevLett.116.214801, URL https://link.aps.org/doi/10.1103/PhysRevLett.116.214801.

[22] A. Adeyemi, Demonstration of Polarized Positrons Based on the Bremsstrahlung of an 8 Mev Polarized Electron Beam (Ph.D. thesis), Graduate College of Hampton University, Hampton, VA, 2022.

[23] P. Adderley, D. Bullard, Y. Chao, C. Garcia, J. Grames, J. Hansknecht, A. Hofler, R. Kazimi, J. Musson, C. Palatchi, K. Paschke, M. Poelker, G. Smith, M. Stutzman, R. Suleiman, Y. Wang, An overview of how parity-violating electron scattering experiments are performed at CEBAF, Nucl. Instrum. Methods Phys. Res. A 1046 (2023) 167710, http://dx.doi.org/10.1016/j.nima.2022.167710, URL https://www.sciencedirect.com/science/article/pii/S0168900222010026.

[24] S. Weinberg, The Quantum Theory of Fields, vol. 1, Cambridge University Press, 1995, http://dx.doi.org/10.1017/CBO9781139644167.

[25] S.B. Gunst, L.A. Page, Compton scattering of 2.62-Mev Gamma rays by polarized electrons, Phys. Rev. 92 (1953) 970–973, http://dx.doi.org/10.1103/PhysRev.92.970, URL https://link.aps.org/doi/10.1103/PhysRev.92.970.

[26] F. Lipps, H. Tolhoek, Polarization phenomena of electrons and photons. II: Results for compton scattering, Physica 20 (1) (1954) 395–405, http://dx.doi.org/10.1016/S0031-8914(54)80054-1, URL https://www.sciencedirect.com/science/article/pii/S0031891454800541.

[27] H.A. Olsen, Application of quantum electrodynamics, in: G. Höhler (Ed.), Springer Tracts in Modern Physics, Volume 44: Ergebnisse Der Exakten Naturwissenschaften, Vol. 44, Springer, Berlin, Heidelberg, 1968, pp. 83–201, http://dx.doi.org/10.1007/BFb0045483.

[28] H. Olsen, L.C. Maximon, Photon and electron polarization in high-energy bremsstrahlung and pair production with screening, Phys. Rev. 114 (1959) 887–904, http://dx.doi.org/10.1103/PhysRev.114.887.

[29] E.A. Kuraev, Y.M. Bystritskiy, M. Shatnev, E. Tomasi-Gustafsson, Bremsstrahlung and pair production processes at low energies, multi-differential cross section and polarization phenomena, Phys. Rev. C 81 (2010) 055208, http://dx.doi.org/10.1103/PhysRevC.81.055208.

[30] E. Voutier, T.S. Bauer, H.W. den Bok, M.E. Brandan, Z. Papandreou, H.W. Willering, Analytical method for polarimeter design optimization, Nucl. Instrum. Methods A 430 (1) (1999) 110–126, http://dx.doi.org/10.1016/s0168-9002(99)00196-5.

[31] ANSYS Electromagnetics Suite, Release 2021 R1. https://www.ansys.com/products/electronics/ansys-maxwell.

[32] D.C. Jones, J. Napolitano, P.A. Souder, D.E. King, W. Henry, D. Gaskell, K. Paschke, Accurate determination of the electron spin polarization in magnetized iron and nickel foils for Møller polarimetry, Nucl. Instrum. Methods A 1043 (2022) 167444, http://dx.doi.org/10.1016/j.nima.2022.167444.

[33] SIMULIA Opera FEA, OPERA-3D User Guide, Version 18R2, 2018, Dassault Systems, Kidlington, U.K. URL https://www.ansys.com/products/electronics/ansys-maxwell.

[34] Alpha Spectra Inc. URL https://alphaspectra.com/.

[35] 3M, URL https://www.3~m.com/3M/en_US/p/d/b5005047091/.

[36] Dupont, URL https://www.dupont.com/brands/tedlar.html.

[37] Hamamatsu, URL https://www.hamamatsu.com/.

[38] X. Li, H. Baumgart, C. Bott, G. Ciovati, S. Gregory, F. Hannon, M. McCaughan, R. Pearce, M. Poelker, H. Vennekate, S. Wang, Design and commissioning of an e-beam irradiation beamline at the Upgraded Injector Test Facility at Jefferson Lab, Nucl. Instrum. Methods Phys. Res. A 1039 (2022) 167093, http://dx.doi.org/10.1016/j.nima.2022.167093, URL https://www.sciencedirect.com/science/article/pii/S0168900222005009.

[39] P.A. Adderley, J. Clark, J. Grames, J. Hansknecht, K. Surles-Law, D. Machie, M. Poelker, M.L. Stutzman, R. Suleiman, Load-locked dc high voltage GaAs photogun with an inverted-geometry ceramic insulator, Phys. Rev. ST Accel. Beams 13 (2010) 010101, http://dx.doi.org/10.1103/PhysRevSTAB.13.010101, URL https://link.aps.org/doi/10.1103/PhysRevSTAB.13.010101.

[40] J. Hansknecht, M. Poelker, Synchronous photoinjection using a frequency-doubled gain-switched fiber-coupled seed laser and ErYb-doped fiber amplifier, Phys. Rev. ST Accel. Beams 9 (2006) 063501, http://dx.doi.org/10.1103/PhysRevSTAB.9.063501, URL https://link.aps.org/doi/10.1103/PhysRevSTAB.9.063501.

[41] G.G. Palacios Serrano, P.A. Adderley, J.M. Grames, C. Hernandez-Garcia, M. Poelker, High-gradient wien spin rotators at Jefferson Lab, 2022, http://dx.doi.org/10.18429/JACoW-NAPAC2022-WEPA20, URL https://www.osti.gov/biblio/1903126.

[42] R. Mair, R. Prepost, H. Tang, E. Garwin, T. Maruyama, G. Mulhollan, Anisotropies in strain and quantum efficiency of strained GaAs grown on GaAsP, Phys. Lett. A 212 (4) (1996) 231–236, http://dx.doi.org/10.1016/0375-9601(96)00058-8, URL https://www.sciencedirect.com/science/article/pii/0375960196000588.

[43] T. Allison, M. Anderson, D. Androić, D. Armstrong, A. Asaturyan, T. Averett, R. Averill, J. Balewski, J. Beaufait, R. Beminiwattha, J. Benesch, F. Benmokhtar, J. Bessuille, J. Birchall, E. Bonnell, J. Bowman, P. Brindza, D. Brown, R. Carlini, G. Cates, B. Cavness, G. Clark, J. Cornejo, S.C. Dusa, M. Dalton, C. Davis, D. Dean, W. Deconinck, J. Diefenbach, K. Dow, J. Dowd, J. Dunne, D. Dutta, W. Duvall, J. Echols, M. Elaasar, W. Falk, K. Finelli, J. Finn, D. Gaskell, M. Gericke, J. Grames, V. Gray, K. Grimm, F. Guo, J. Hansknecht, D. Harrison, E. Henderson, J. Hoskins, E. Ihloff, K. Johnston, D. Jones, M. Jones, R. Jones, M. Kargiantoulakis, J. Kelsey, N. Khan, P. King, E. Korkmaz, S. Kowalski, A. Kubera, J. Leacock, J. Leckey, A. Lee, J. Lee, L. Lee, Y. Liang, S. MacEwan, D. Mack, J. Magee, R. Mahurin, J. Mammei, J. Martin, A. McCreary, M. McDonald, M. McHugh, P. Medeiros, D. Meekins, J. Mei, R. Michaels, A. Micherdzinska, A. Mkrtchyan, H. Mkrtchyan, N. Morgan, J. Musson, K. Mesick, A. Narayan, L. Ndukum, V. Nelyubin, Nuruzzaman, W. van Oers, A. Opper, S. Page, J. Pan, K. Paschke, S. Phillips, M. Pitt, M. Poelker, J. Rajotte, W. Ramsay, W. Roberts, J. Roche, P. Rose, B. Sawatzky, T. Seva, M. Shabestari, R. Silwal, N. Simicevic, G. Smith, S. Sobczynski, P. Solvignon, D. Spayde, B. Stokes, D. Storey, A. Subedi, R. Subedi, R. Suleiman, V. Tadevosyan, W. Tobias, V. Tvaskis, E. Urban, B. Waidyawansa, P. Wang, S. Wells, S. Wood, S. Yang, S. Zhamkochyan, R. Zielinski, The Qweak experimental apparatus, Nucl. Instrum. Methods Phys. Res. A 781 (2015) 105–133, http://dx.doi.org/10.1016/j.nima.2015.01.023, URL https://www.sciencedirect.com/science/article/pii/S0168900215000509.

[44] N.F. Mott, The scattering of fast electrons, Proc. R. Soc. Lond. 124 (1929) 425–442, http://dx.doi.org/10.1098/rspa.1929.0127.

[45] T.J. Gay, F.B. Dunning, Mott electron polarimetry, Rev. Sci. Instrum. 63 (2) (1992) 1635–1651, http://dx.doi.org/10.1063/1.1143371.

[46] N. Sherman, Coulomb scattering of relativistic electrons by point nuclei, Phys. Rev. 103 (1956) 1601–1607, http://dx.doi.org/10.1103/PhysRev.103.1601, URL https://link.aps.org/doi/10.1103/PhysRev.103.1601.

[47] X. Roca-Maza, Personal communication, 2021.

[48] X. Roca-Maza, Theoretical calculations for precision polarimetry based on Mott scattering, Europhys. Lett. 120 (3) (2018) 33002, http://dx.doi.org/10.1209/0295-5075/120/33002.

[49] H. Wegener, Mott-streuung an streufolien endlicher dicke, Zeitschrift für Physik 151 (3) (1958) 252–263, http://dx.doi.org/10.1007/BF01338381, https://doi.org/10.1007/BF01338381.

[50] Lebow Company. URL https://lebowcompany.com/.

[51] J.M. Grames, C.K. Sinclair, M. Poelker, X. Roca-Maza, M.L. Stutzman, R. Suleiman, M.A. Mamun, M. McHugh, D. Moser, J. Hansknecht, B. Moffit, T.J. Gay, High precision 5 MeV Mott polarimeter, Phys. Rev. C 102 (2020) 015501, http://dx.doi.org/10.1103/PhysRevC.102.015501, URL https://link.aps.org/doi/10.1103/PhysRevC.102.015501.